Xiaobo Zhang
Huasheng Gan
Huazheng Xue
Qing Jiang ✉

https://doi.org/10.21278/TOF.483057623
ISSN 1333-1124
eISSN 1849-1391

NUMERICAL SIMULATION OF AN EXPERIMENTAL STUDY ON STRUCTURE OPTIMIZATION FOR COMPARTMENT DRYERS

Summary

Compartment dryers for fruits and vegetables involve problems including dead zones and nonuniform drying. To address these problems, experimental and numerical analyses are carried out in this study using an airflow control equation and the k-omega SST model to optimize the structural parameters of the drying section in the compartment dryer. The dryer was numerically simulated using Fluent software, and the dryer structural parameters (i.e., numbers of hot-air inlets and outlets, aperture size, and tilt angle) were optimized using response surface analysis. Subsequently, the airflow distribution within the dryer was determined by using Fluent software; the temperature nonuniformity coefficient (M_t), the velocity nonuniformity coefficient (M_v), the temperature deviation ratio (E_t), and the velocity deviation ratio (E_v) served as evaluation metrics for airflow uniformity in the dryer. The results revealed that M_t, M_v, E_t, and E_v decreased by 25.47%, 30.49%, 28.41%, and 14.74%, respectively, enhancing the airflow uniformity in the dryer.

Key words: *dryer, numerical simulation, structure optimization, uniformity*

1. Introduction

Compartment dryers are predominantly used for baking fruits and vegetables (e.g., mushrooms) in agricultural engineering. However, due to high energy consumption and complicated heat and mass exchange processes, conventional compartment dryers used for drying fruits and vegetables pose many challenges, such as the uneven distribution of heat fields and the drying dead angle. These issues are usually related to weather conditions, specific qualities of individual fruits and vegetables, the setting of equipment parameters, and the complicated drying process [1, 2, 3]. In addition, the internal physical properties and chemical compositions of fruits and vegetables will be changed during the drying process; such changes are closely associated with heat and mass transfer dynamics. Generally speaking, dryers for fruits and vegetables should meet the following two requirements: (i) the internal moisture from fruits and vegetables needs to be removed effectively, and (ii) the nutritional content of the fruits and vegetables needs to be preserved during drying [4]. Therefore, the shape design of the dryer and the optimization of drying process parameters are crucial to the enhancement of the drying performance of fruits and vegetables [5].

In recent years, numerous scholars have used computational fluid dynamics (CFD) models to study agricultural product dryers. The CFD models are cost-effective and efficient, enabling the rapid derivation of speed, temperature, pressure, and other parameters across various temporal and spatial distributions [6, 7]. This can help scholars study the patterns and principles governing the movement of fluids within agricultural product dryers [8, 9, 10]. Yue et al. studied the effect of different flow parameters on the airflow distribution inside the multilayer mesh belt dryer by obtaining its velocity distribution through numerical simulation and verifying it through experiments to get a better optimization scheme and solve problems such as the uneven distribution of model airflow [11]. Zhang combined the CFD model with experimental validation to investigate the effects of transporter position, airflow moisture, and different feed thicknesses inside the dryer on the airflow uniformity on the dryer surface. It was found that changing the structure produced a better air equalization effect [12, 13, 14]. In [15-16], Huang D. et al. used Fluent software to study the effect of drying characteristics and the quality of oil tea seeds through different key parameters, such as temperature, load density, heating time, and the length of intermittent time. The studies have shown that when the flow parameters are in line with the drying requirements, a better drying flow environment can be provided, which contributes to material drying and energy savings. Li et al. used the LES model for numerical simulation of the dryer and optimized its structure. When the velocity is 1.5 m/s and the transverse and longitudinal ratios are small, the fluctuation of the heat flow field is small, and the temperature uniformity reaches a certain degree of improvement [17]. Ye Zhang et al. explored the application of multi-objective genetic algorithms in the design and optimization of heat exchangers by considering five design variables, such as hot tube diameter, transverse pitch, longitudinal pitch, cold flow velocity, and hot flow velocity, for simultaneous optimization. The application of multi-objective optimization in CFD models was thus demonstrated [18]. At present, the optimization of compartment dryers is focused on single-factor optimization without considering the different dryer structures at the same time to optimize the joint effect on the overall flow field uniformity of the dryer [19, 20, 21]. In the studies dealing with the dryer flow field uniformity, there are still problems to be solved, such as poor flow field uniformity, low drying efficiency, and uneven drying quality of the impingement dryer.

This paper describes the chamber dryer and addresses the most widespread problems with the current Chinese fruit and vegetable chamber dryer to provide uniformity and quality of drying as a starting point. The analysis of the distribution of hot airflow throughout the drying part of the dryer was done specifically using Fluent simulation software. Based on the simulation results, the study identified optimization schemes for the number of air inlets and outlets, aperture size, and tilt angle in the drying section. Additionally, temperature and velocity deviation ratios, as well as temperature and velocity nonuniformity coefficients, were examined using single-factor analysis and multi-objective optimization. An experimental platform was established for validation, confirming that the optimized compartment dryer exhibited enhanced drying efficiency. The simulation and experimental results can serve as a reference for the structural optimization and design of compartment dryers.

2. Numerical Simulation

2.1 Establishment of a model

In this study, a three-dimensional (3D) model of a compartment dryer, whose structure is shown in Figure 1, is established. The model was considered to have two air inlets and outlets securely positioned at both ends, with multiple grid-drying racks assembled within the drying section. Figure 2 shows the structure of two air inlets and outlets, and Fig. 3 shows the structure of the grid drying rack and material. For efficient CFD processing and to meet the simulation

requirements and speed up the software calculator, the 3D model was made simpler using SolidWorks software. Ignoring the flow field simulation did not significantly affect the small, complex geometric features. The simplified computational domain model includes the drying chamber wall, air inlet, return air inlet, and porous media layer. The simplified model measured 10,100 mm in length, 3000 mm in width, and 2000 mm in height.

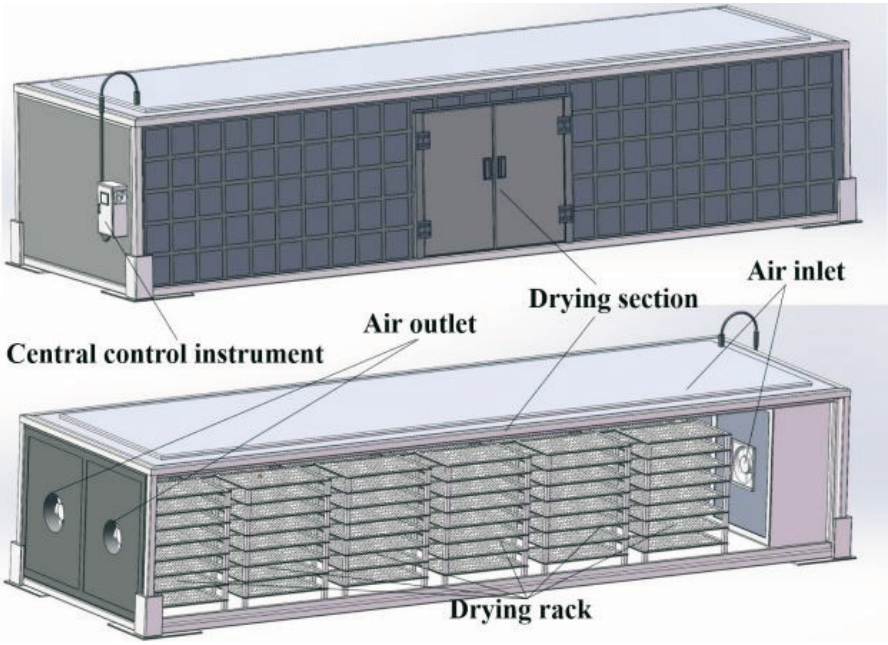

Fig. 1 Structure diagram of the drying oven

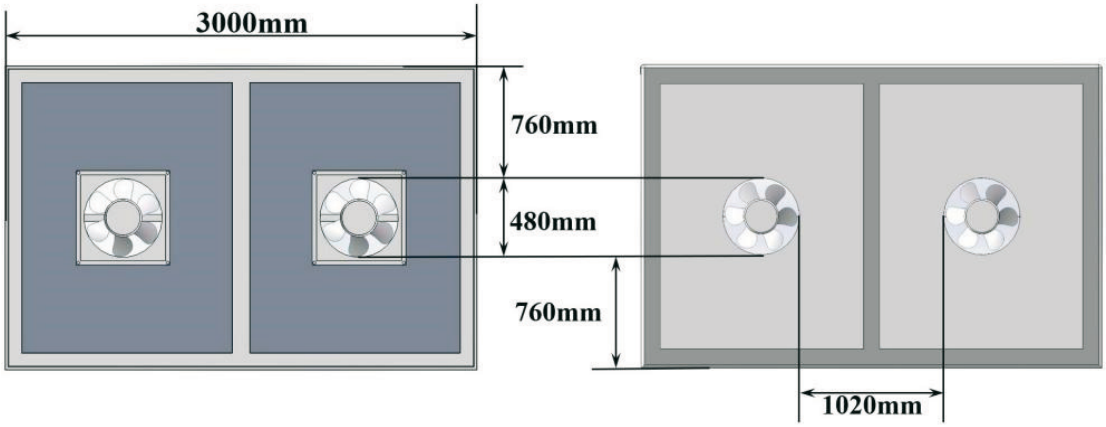

Fig. 2 Structure diagram of air inlets and outlets

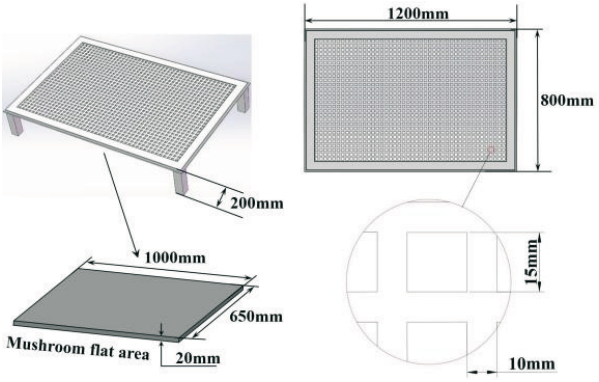

Fig. 3 Structure diagram of the drying rack and material

2.2 Mathematical model

In the course of the study, the principles of mass conservation, energy conservation, and momentum conservation are all satisfied by the flow state [22, 23, 24]. The continuum equation embodies the law of conservation of mass in CFD, followed by the energy equation. Considering the mushroom layer as a porous medium, numerical simulation of the mushroom dryer drying box is carried out using Fluent software with the Semi-Implicit Method for Pressure Linked Equations (SIMPLE) algorithm, and the finite volume method is used to discretize governing equations [25, 26]. The k-omega SST model first proposed by Menter F. R. has the advantages of wide applicability, high computational accuracy and stability, which were obtained by experiments, and high computational efficiency [27, 28, 29]. In the drying process, the inlet wind speed of the drying box is 1m/s and above, and the Reynolds number is greater than or equal to 5.6×10^4, so the flow inside the drying chamber is turbulent. The continuity equation and the momentum equation are shown in Eqs. (1) and (2), respectively.

$$\nabla \bullet u = 0 \tag{1}$$

$$\nabla u + \nabla \bullet (uu) = -\frac{1}{\rho_g}\nabla P + \nabla \bullet \left[\left(v_g + v_T \right) \left(\nabla u + \left(\nabla u \right)^T \right) \right] + F, \tag{2}$$

where u is the vector wind speed (m/s), ρ_g is the density of hot air (kg/m^3), p is the relative pressure inside the drying oven, v_g is the kinematic viscosity of hot air (m^2/s), v_T is the turbulent viscosity of hot air, and F the momentum source term.

In the free-flow region, there is no additional resistance to the hot air, so the momentum source term F in this region is zero. In the mushroom lay-flat region, since it is set as a porous medium, the flow of hot air is affected by the resistance of the porous medium. According to the Darcy-Forchheimer law, the resistance to flow within the porous medium is divided into two parts: viscous resistance, which is proportional to the velocity of flow, and inertial resistance, which is proportional to the square of the velocity of flow. Ergun's formula is used to calculate the momentum source term F.

$$F = -\left(v_g \frac{150\left(1-\varphi^2\right)}{d_{eq}^2 \varphi^3} + \frac{1}{2}|u| \frac{3.5\left(1-\varphi\right)}{d_{eq}\varphi^3} \right) u, \tag{3}$$

where φ is porosity and d_{eq} is the equivalent diameter(m).

In the mushroom lay-flat region, the number of mushrooms on a drying rack is between 530 and 640, and the pores between the mushrooms are full of air, so this region is assumed to be a porous medium, consisting of hot air and mushrooms. The mushrooms are assumed to be solids, the hot air is an incompressible ideal gas, and the effect of gravity is not taken into account due to the high velocity of the air flow, which is dominated by forced convection. [30, 31]. The specific values of the physical parameters are shown in Table 1 [32].

Table 1 Physical parameters adopted in the model of material oven integration.

Initial mass fraction of water vapour ω_0	Mass fraction of water vapour in incoming air ω_{in}	Density of solid substrate in mushrooms ρ_s/(kg/m^3)	Density of liquid water in mushrooms ρ_w/(kg/m^3)
0.007798	0.0345	1591	998
Density of air in mushroom pores ρ_g/(kg/m^3)	Thermal conductivity of solid substrate of mushrooms λ_s/(W/(m·°C))	Thermal conductivity of liquid water in mushrooms λ_w/(W/(m·°C))	Thermal conductivity of air in mushroom pores λ_g/(W/(m·°C))
1.007	0.1	0.59	0.026
Specific heat capacity of solid substrate of mushrooms C_{ps}/(J/(kg·°C))	Specific heat capacity of liquid water in mushrooms C_{pw}/(J/(kg·°C))	Specific heat capacity of air in mushroom pores C_{pg}/(J/(kg·°C))	Initial wet substrate water content M_{w0}/(kg·kg)
1500	4182	1006	0.8856
Kinematic viscosity of air v_g/(m/s^2)	Latent heat of evaporation L/(J/kg)	Initial porosity φ	Diffusion coefficient D_{va}/(m^2/s)
1.778	2.26×106	0.59	2.6×10
Initial equivalent diameter d_{ep0}/m	Initial interfacial area density A_{lg0}/(1/m)	Initial volume fraction of solid substrate in shiitake mushrooms φ_{s0}	Initial volume fraction of liquid water in shiitake mushrooms φ_{w0}
0.0195	86.6	0.05	0.457

2.3 Analysis of heat flow field simulation results

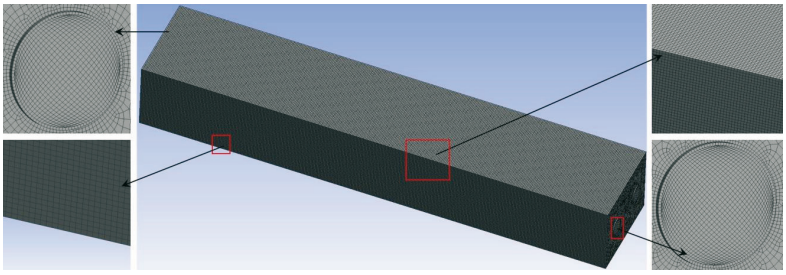

Fig. 4 Dryer grid model diagram

The model and mesh were generated using ICEM 21.0 and checked using Richardson extrapolation, indicating an asymptotic value of 0.9704, which is within the range of convergence. The meshing model of the dryer is shown in Fig. 4. Internal air for the steady state viscous flow in the fruit and vegetable compartment dryer is approximated as an incompressible ideal gas because of the low flow rate and minimal density change. The maximum drying temperature of a compartment dryer is generally 55 °C. The direction of the incoming air is typically perpendicular to the inlet boundary and is uniformly distributed. The temperature for each inlet can be adjusted according to the requirements of the drying process for the material. In this study, the velocity at the inlet boundary condition was set to 8 m/s, and the temperature was set to 55 °C (328.15 K).

The outlet conditions were set as follows: outlet pressure, 0 Pa; wall thickness, 2 mm; and return flow, no flow. Figure 5 shows cloud diagrams of the hot air temperature and velocity distributions at the following cross-sections of the dryer: X = 2020 mm, X = 4040 mm, X = 6060 mm, and X = 8080 mm. This figure shows notable differences in temperature and velocity across the various cross-sections.

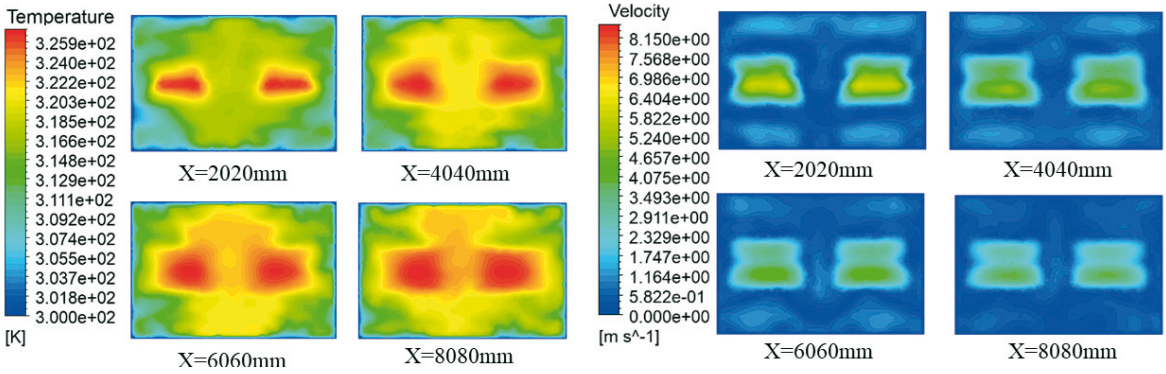

(a) X-axis temperature field distribution (b) X-axis velocity field distribution

Fig. 5 Model simulation results

Specifically, in the horizontal cross-sectional direction, airflow velocities were relatively low both above and below the position of the air inlet, as shown in Fig. 5(a). However, the temperature of the hot air was elevated near the air inlet. As the hot air progressed, it expanded predominantly above the drying section. Notably, a low-velocity zone was observed at the corners of the drying section, effectively creating a dead zone; this resulted in a nonuniform velocity distribution. The constraints posed by the positioning of the air inlet and outlet and the quality of the material could hinder the flow of hot air in specific regions, potentially compromising drying quality. As shown in Fig. 5(b), the temperature and airflow velocity were relatively high in the middle region of the drying section. A possible explanation for this phenomenon is that the presence of the grille drying rack impeded the vertical circulation of the heat flow, and the level of circulation between the grilles was inadequate, causing certain sections of the grille drying rack to experience either excessively high or low temperatures and airflow velocities. In this study, considerable variations in temperature and airflow velocity across each cross-section were also noted. The distribution of hot air throughout the circulation area was not uniform, resulting in considerable nonuniformity in both temperature and airflow velocity distributions.

3. Analysis and Discussion of Results

To clearly determine the pressure and the distributions of temperature and air velocity within the drying section of the compartment dryer, the following metrics were used in this study: the temperature nonuniformity coefficient M_t, the velocity nonuniformity coefficient M_v, the temperature deviation ratio E_t, and the velocity deviation ratio E_v. These metrics were used to quantitatively assess the uniformity of temperature and air velocity within the drying section [33]. Notably, lower values of M_t, M_v, E_t, and E_v typically indicate superior drying uniformity within the drying section.

$$M_t = \frac{\sqrt{\frac{1}{n}\sum_{i=1}^{n}(t_i - \bar{t}_a)^2}}{\bar{t}_a} \times 100\% \tag{4}$$

$$M_v = \frac{\sqrt{\frac{1}{n}\sum_{i=1}^{n}(v_i - \bar{v}_a)^2}}{\bar{v}_a} \times 100\% \tag{5}$$

$$E_t = \frac{\bar{t}_{out} - \bar{t}_a}{\bar{t}_a} \times 100\% \tag{6}$$

$$E_v = \frac{\bar{v}_{out} - \bar{v}_a}{\bar{v}_a} \times 100\% \tag{7}$$

In the equations listed above, $\bar{t}_a$ and $\bar{v}_a$ represent the temperature and the airflow velocity at the *i*th monitoring point, respectively; *a* and *b* represent the average temperature and the airflow velocity, respectively; $\bar{t}_{out}$ and $\bar{v}_{out}$ represent the average temperature and the airflow velocity at the outlet, respectively; and *n* represents the number of monitoring points (i.e., the number of monitoring points in the plane of the simulation model or the drying section of the compartment dryer). In this study, a total of 24 monitoring points were considered at each of the following cross sections (Fig. 6): Y = 500 mm, Y = 1000 mm, Y = 1500 mm, Y = 2000 mm, and Y = 2500 mm.

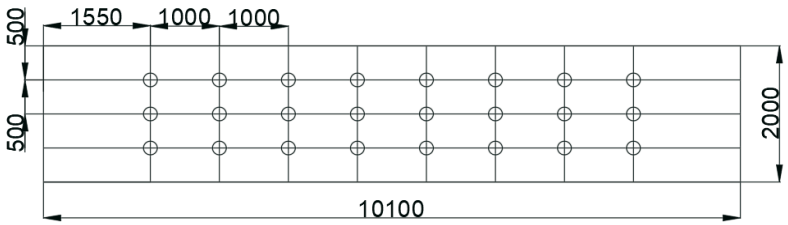

Fig. 6 Distribution of cross-section monitoring points in the drying section

3.1 Single-factor analysis for the compartment dryer

A single-factor analysis was performed in this study to determine the optimal number of air inlets and outlets in the drying section of the compartment dryer to mitigate the inconsistent air distribution in the drying section. Specifically, optimizing the number of air inlets and outlets could address the problem of uneven airflow distribution in the drying section of the compartment dryer, particularly above and below the air inlet, and the considerable disparities in the airflow velocity across each layer. In the optimization process, several air intake and air outlet numbers are considered, with the number of design schemes for both being 1, 3, 4, 5, 6, 7, 8, and 9. In addition, the grille aperture size was also optimized to address the uneven circulation of hot air within the grille and the rapid reduction in temperature and airflow velocity as the hot air advances. This optimization could enable the hot air to circulate vertically through the bottom aperture of the grille, ameliorating airflow inconsistencies near the grille. The original aperture of the grille frame had a size of 15 × 15 mm; however, the following aperture sizes were analysed in this study: 11 × 11, 12 × 12, 13 × 13, 14 × 14, 16 × 16, 17 × 17, 18 × 18, and 19 × 19 mm. Finally, to address the problem of uneven drying within the compartment dryer, the tilt angle of the grille was optimized to ensure that the airflow of the heat source was more uniformly distributed. The following tilt angles were considered in this study: 1°, 2°, 3°, 4°, 5°, 6°, 7°, and 8°. The number of air intakes, the number of air vents, the aperture size, and the tilt angle are denoted by P1, P2, P3, and P4, respectively, and the output parameters of the

project are M_t, M_v, E_t, and E_v, which are denoted by P5, P6, P7, and P8, respectively. The optimization analyses were conducted using Fluent software, and each group of simulations was carried out three times. The results are averaged and shown in Fig. 7.

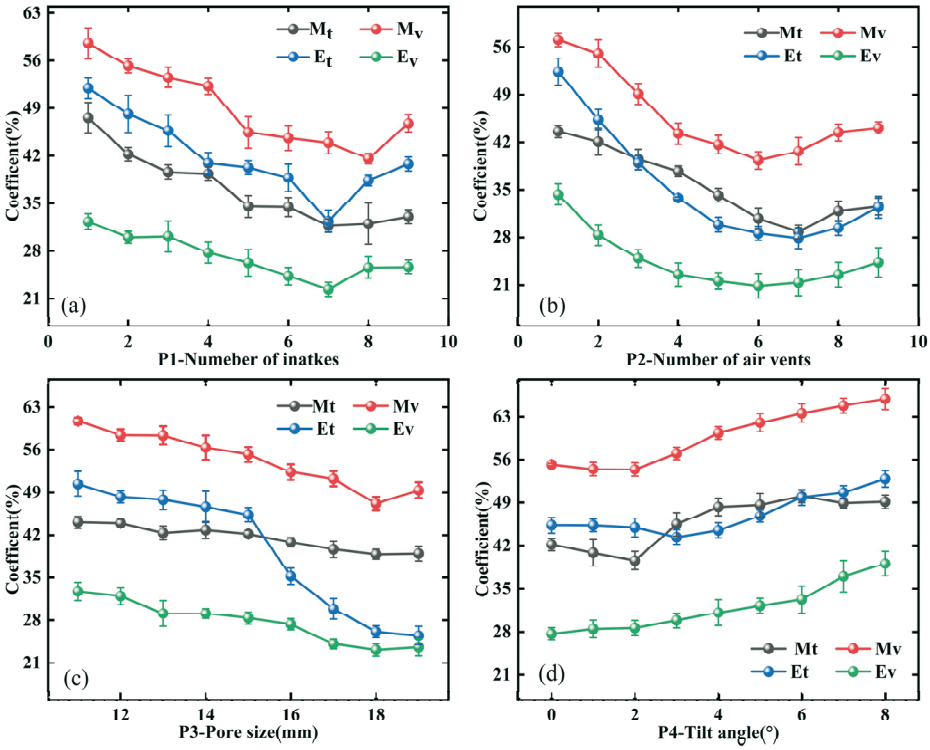

Fig. 7 Analysis of the results of different design options

The results shown in Fig. 7(a) indicated that the optimal schemes for determining the appropriate number of air inlets were the numbers 6, 7, and 8 (denoted as a1, a2, and a3, respectively). Similarly, Fig. 7(b) shows that the optimal schemes for determining the appropriate number of air outlets were the numbers 6, 7, and 8 (denoted as b1, b2, and b3, respectively). Figure 7(c) shows that the optimal schemes for pore size were obtained for sizes of 17 × 17, 18 × 18, and 19 × 19 mm. The associated M_t, M_v, E_t, and E_v values were reduced by 6.2%, 8.07%, and 7.93%; 7.26%, 14.65%, and 10.65%; 37.99%, 45.71%, and 47.1%; and 19.67%, 22.96%, and 20.46%, respectively, when compared to the original modelling scenario. From Fig. 7(d), one can see that the uniformity of the flow field distribution is relatively better at tilt angles of 0°, 1°, and 2°, which are the relatively optimal parameters.

Considering the optimal numbers of air inlets and outlets, nine simulation schemes were designed in this study. These were modelled and input into Fluent software for fluid simulation analysis, and the results are shown in Fig. 8. Schemes a1b1, a1b2, and a1b3 exhibited the greatest reductions in M_v in the drying section, with reductions of 19.18%, 19.07%, and 19.97%, respectively, compared to the original model. With small fluctuation intervals of the error bars and few outliers, the data have strong stability, and programs a1b1, a1b2, and a1b3 have the largest reduction in M_v in the drying section.

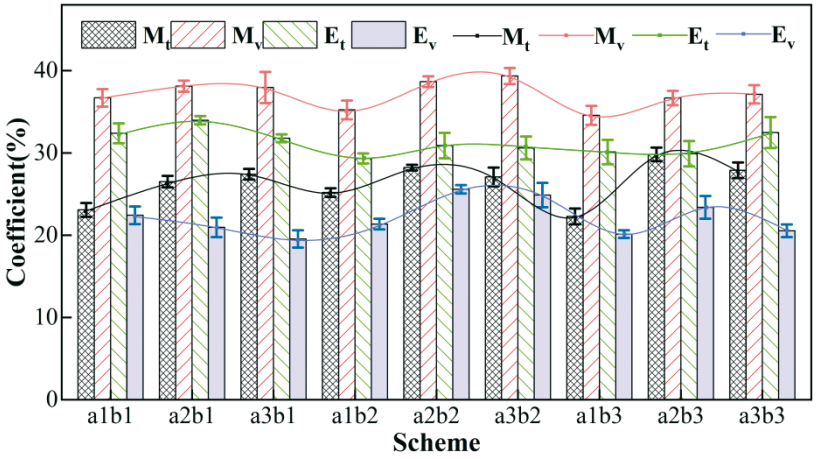

Fig. 8 Optimization results of the number of air inlets and outlets

3.2 Multi-objective optimization of the compartment dryer

According to the preceding simulation results, the number of air inlets and outlets, the aperture size, and the tilt angle of the grille significantly influenced the turbulence distribution within the dryer. Therefore, an orthogonal simulation experiment was used in this study, selecting the number of air outlets (A), the aperture size (B), and the grille tilt angle (C) as the three primary factors for analysis. The parameters for these factors across three levels are presented in Table 2.

Table 2 Orthogonal test factor level table

Horizontal factors	Factor		
	P2-Number of air vents	P3-Pore size (mm)	P4-Tilt angle (°)
1	6	17	0
2	7	18	1
3	8	19	2

According to the orthogonal test principle, the most representative parameter groups should be selected to determine the factors and specific parameters for the orthogonal test. The input variables are adjusted to an appropriate status for the purpose of optimizing the responses to their ideal position [34]. Thus, the orthogonal simulation experiment is carried out in this study to examine the flow field in the compartment dryer; the three factors across three levels are considered. The parameters for this experiment were inputted into Design-Expert 8.0.6.1, and 13 distinct orthogonal test point groups were obtained. These were subsequently introduced into the corresponding M_t, M_v, E_t, and E_v models. The Box-Behnken response surface analysis method was applied to the key parameters, yielding a regression model with a P value of <0.01. Misfitting terms are all greater than 0.5, indicating that M_t, M_v, E_t, and E_v were highly significant for the regression model and non-significant for the misfit term. Simulations were conducted on the initial data, and the results were visualized graphically. The results indicated that the drying of fruits and vegetables primarily relies on the airflow velocity of the thermofluid within the drying section to elevate the temperature of the produce and evaporate its moisture. Among the variables studied, M_v had the most significant impact on the drying process. A two-by-two analysis was conducted to determine the effects of the numbers of air inlets and outlets, tilt angle, and aperture size on M_v.

Taking the increase in M_v as the corresponding index, the corresponding surface variation of the interaction between the number of air outlets, the pore size, and the tilt angle is shown in Fig. 9, and the input parameter of each non-participating response surface is the initial value of the dryer.

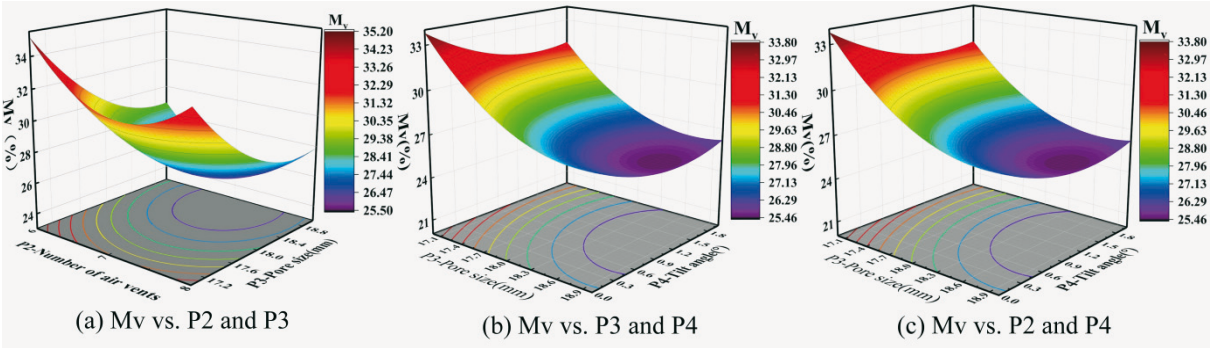

Fig. 9 Analysis of M_v - corresponding surface results

Figure 9(a) shows the response surface of M_v when the number of air outlets and the pore size work together. When the number of air outlets is between 6 and 8, M_v decreases and then increases with the increase in pore size; when the pore size is between 17 and 19 mm, M_v decreases and then increases with the increase in the number of air outlets. The minimum response value reached by M_v is 25.71% when P2 = 7 and P3 = 18.58 mm. Figure 9(b) shows the M_v response surface for the combined effect of pore size and tilt angle. When the pore size is between 17 and 19 mm, M_v decreases and then increases with the tilt angle; when the tilt angle is between 0 and 2°, M_v decreases and then increases with the pore size. The minimum response value reached by M_v is 24.82% when P3 = 18.32 mm and P4 = 1.37°. Figure 9(c) shows the M_v response surface for the combined effect of the number of air outlets and the tilt angle. Between 6 and 8, M_v decreases and then increases with the increase in the tilt angle; between 0 and 2°, M_v decreases and then increases with the increase in the number of air outlets. The minimum response value reached by M_v is 25.66% when P2 = 7 and P4 = 1.37°.

After the response surface analysis, a fit test was done to ascertain the accuracy of response surface analysis-based predictions and compare them with experimental values. The fit test datas must be normalized owing to varying M_t, M_v, E_t, and E_v ranges. Take the normalized velocity nonuniformity coefficient as an example:

$$Normalization = \frac{M_{vi} - M_{v\min}}{M_{v\max} - M_{v\min}} \tag{8}$$

In Figure 10, the horizontal axis represents normalized design point observations, and the vertical axis represents the normalized predicted values from the response surface analysis. The design points in the figure indicate the ratio of predicted to observed values at those points. The discrete points in the figure represent the ratio between the predicted response surface value and the observed value at the design point: the closer the discrete points are to the diagonal line, the better the predicted response surface point fits the test point. As shown in Fig. 10, the response surface analysis-based predictions for the four output parameters aligned closely with the diagonal demonstrate the accuracy of the simulation.

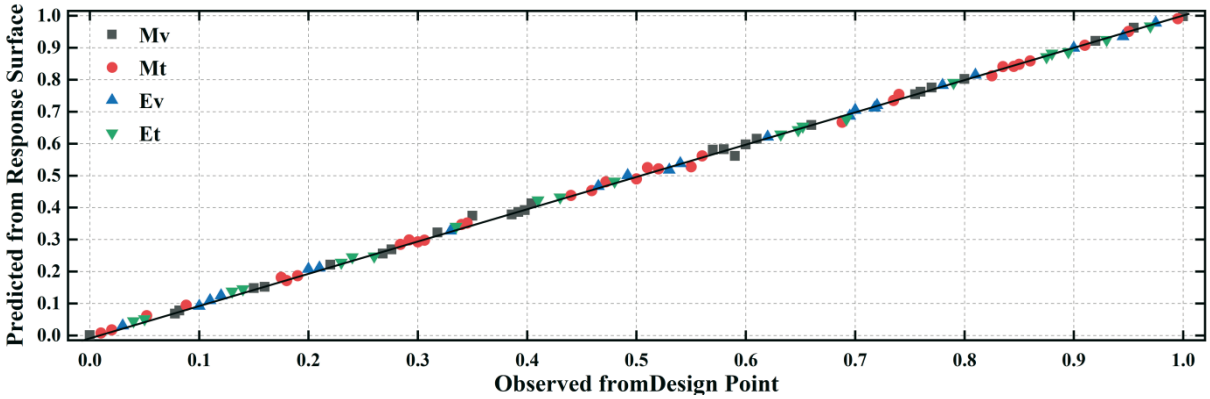

Fig. 10 Fitting degree of output parameters

A sensitivity analysis is carried out to further validate each model and examine the contribution of an input variable to the output for each case in the training data [35]. Local sensitivity reflects the degree of the relationship between output and input parameters. A higher local sensitivity level indicates a stronger relationship between input and output parameters [36, 37, 38]. Take the sensitivity of the velocity nonuniformity coefficient as an example:

$$Sensitivity = \frac{M_{v\max} - M_{v\min}}{M_{vave}} \tag{9}$$

A local sensitivity analysis was carried out in this study, and the results obtained for each input parameter are shown in Fig. 11. As shown in this figure, p1 had the greatest effect on M_t, and p2 had the greatest effect on M_t, M_v, E_t, and E_v. Simulation was done to determine the optimal values.

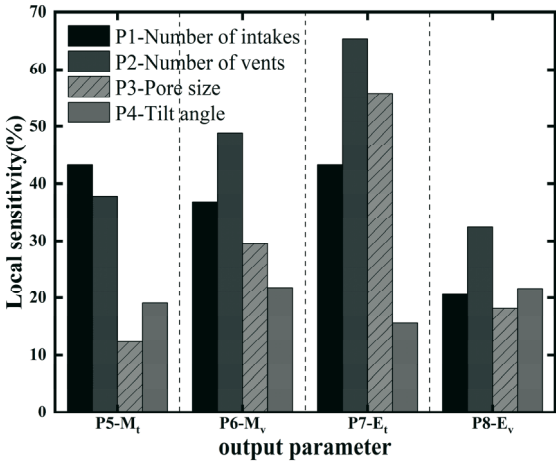

Fig. 11 Local sensitivity of output parameters

The Design-Expert model was used to identify the optimal parameter combination that resulted in the largest reduction in the velocity nonuniformity coefficient. The model showed that the following combination resulted in the largest reduction in the velocity nonuniformity coefficient: number of air outlets, 7; aperture size, 18.25 × 18.25 mm; and tilt angle, 1.16°. When this combination was used, the values for M_t, M_v, E_t, and E_v were 16.43%, 24.56%, 19.29%, and 14.65%, respectively. To validate the reliability of these results, the optimization results were remodelled, the mesh was partitioned, and parameters were computed. The derived temperature and velocity nonuniformity coefficients and temperature and velocity deviation ratios were compared with Fluent validation results. The validation results for M_t, M_v, E_t, and E_v were 16.78%, 24.74%, 19.74%, and 15.46%, respectively, with the corresponding errors being 2.13%, 0.73%, 2.33%, and 5.23%; the maximum error was 5.23%. These results confirmed the accuracy of the response surface analysis.

Figure 12 shows cloud diagrams of the temperature and airflow velocity distributions obtained for the optimized compartment dryer at the following cross sections: X = 2020 mm, X = 4040 mm, X = 6060 mm, and X = 8080 mm. According to this figure, the original model of the dryer exhibited substantial variations in airflow velocity in the horizontal direction of the compartment dryer. The distribution of airflow velocity in the drying section was not uniform. However, the optimization of the structural parameters of the compartment dryer, particularly the number of air inlets and outlets, substantially enhanced the uniformity of the airflow velocity within the compartment dryer. Altering the aperture size facilitated the more complete circulation of the hot air in and out of the grille, substantially improving the airflow velocity uniformity. Adjusting the tilt angle of the grille ensured comprehensive contact between the materials on the grille and the hot air. Under this optimized drying condition, M_t, M_v, E_t, and E_v were reduced from 42.25%, 55.23%, 48.15%, and 30.2% to 16.78%, 24.74%, 19.74%, and 15.46%, respectively.

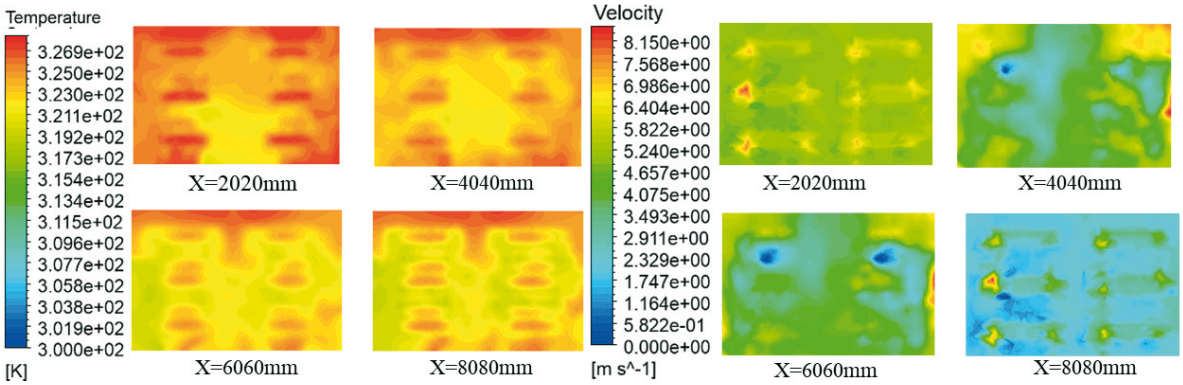

(a) X-axis temperature field distribution (b) X-axis velocity field distribution

Fig. 12 Model simulation results

3.3 Test of a physical model of the compartment dryer

Because of experimental limitations, in this study, a physical model of the compartment dryer was established at a scale 10 times smaller than that of the 3D simulation model. The physical model was tested using the following equipment: a compartment dryer, a centrifugal fan, a Sigma AR866 airflow velocity tester, mushrooms, and a power supply line. A detailed setup is shown in Fig. 13.

Fig. 13 Test site photo

The inlet airflow velocity is a crucial parameter for systematic testing. A test to determine the effect of varying airflow velocities on the performance of the dryer was done; the focus was on the maintenance of fan stability. The centrifugal fan used in the test had 10 distinct settings. For each setting, the airflow velocity was measured 10 times at 10-second intervals. The average of the measurement results was taken as the representative airflow velocity for that particular setting. As shown in Fig. 14, a linear relationship between fan frequency and airflow velocity magnitude was observed.

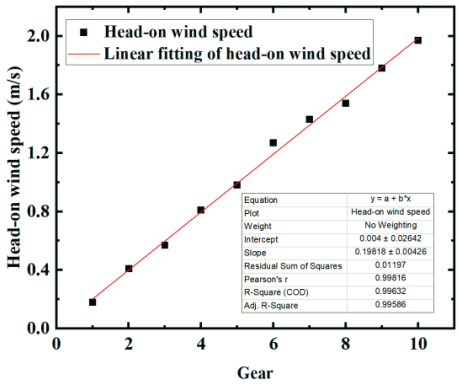

Fig. 14 Test of the wind speed control performance stability

Owing to the structural constraints of the testing platform, the airflow velocity values for two cross sections (i.e., Y = 1000 mm and Y = 2000 mm, as described in Section 2.1), were proportionally scaled down by a factor of 10 for the test. For this test, settings 2, 4, 6, and 8 of the centrifugal fans were chosen as test conditions. An airflow velocity fitting curve was plotted, and the curve was used to calculate the average airflow velocities for the selected conditions; specifically, the average airflow velocities for settings 2, 4, 6, and 8 were 0.41, 0.81, 1.27, and 1.54 m/s, respectively. The corresponding experimental results are shown in Fig. 15.

Table 3 Comparison of test and simulation M_v and E_v errors

Fan gear	M_v experimental value (%)	M_v artificial value (%)	M_v error (%)	E_v experimental value (%)	E_v artificial value (%)	E_v error (%)
2	17.43	18.69	7.22	15.32	15.43	0.78
4	18.37	19.08	3.86	14.87	15.26	2.62
6	17.67	17.78	0.62	14.75	15.14	2.65
8	18.95	19.3	1.85	15.24	15.66	2.76

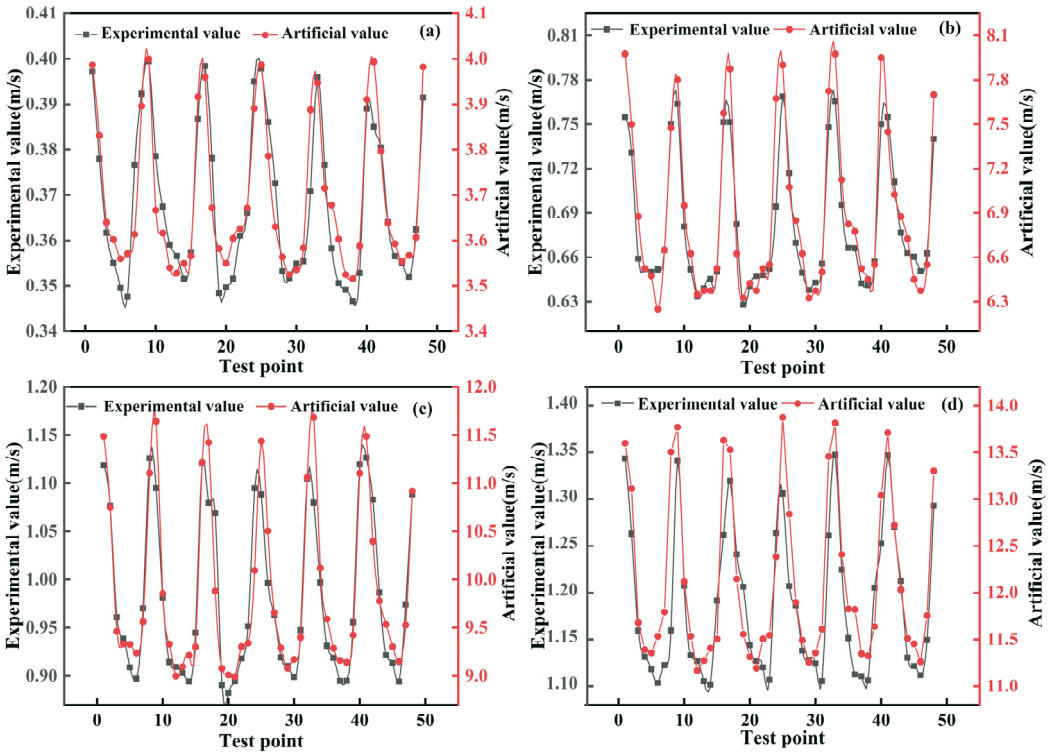

Fig. 15 Comparison of wind speeds between test and simulation

The primary objective of the experimental data processing was to derive optimized structures for the compartment dryer and to juxtapose the numerical simulation results to validate their accuracy. The data in Fig. 13 were analysed, yielding the results presented in Table 3. The average discrepancy between the simulation and experimental values of M_v under the given dryer conditions was 3.39%, with the maximum divergence reaching 7.22%. The average error between the simulation and experimental values of E_v was 2.19%, and the greatest discrepancy was 2.76%. Notably, these errors were all within a 10% margin, satisfying typical experimental tolerances. This reciprocity between the experimental and simulation results aligns well with real-world scenarios, further corroborating the precision of the simulation outcomes.

4. Conclusions

(1) In this model, the CFD method is employed to predict the airflow field of the compartment dryer. The temperature nonuniformity coefficient, the velocity nonuniformity coefficient, the temperature deviation ratio, and the velocity deviation ratio were used as evaluation metrics for the optimization of the compartment dryer. The fluent-based numerical simulations reveal that the optimized compartment dryer exhibited notably uniform temperature and airflow velocity distributions in its drying section compared with the unoptimized one, and the uniformity of airflow within the drying section was improved dramatically.

(2) Single-factor analysis results indicate that the optimization of the numbers of air inlets and outlets, the aperture size, and the grille tilt angle resulted in substantial reductions in M_t, M_v, E_t, and E_v. Multi-objective optimization revealed the optimal design parameter combination: numbers of air inlets and outlets, 6 and 7, respectively; aperture size, 18.25 × 18.25 mm; and tilt angle, 1.16°. Compared with the initial structural parameters, the optimized parameters led to 25.47%, 30.49%, 28.41%, and 14.74% reductions in M_t, M_v, E_t, and E_v, respectively.

(3) Additionally, a test platform and experimental testing were established, and tests were done to corroborate the accuracy of the compartment dryer in numerical simulation, which demonstrates that the average error for M_v was 3.39% and that for E_v, was 2.19%, which is in agreement with the accuracy and reliability of the simulations obtained by comparing the experimental values with the simulation ones.

REFERENCES

[1] Chibuzo N S, Osinachi U F, Janes M T, et al. Technological advancements in the drying of garden stuff: A review. African Journal of Food Science, 2021, 15(12): 367-79.

[2] Exell R. Basic design theory for a simple solar rice dryer. International Energy Journal, 2017, 1(2). 8-15.

[3] Yue X, Zhao J, Shi E, et al. Analysis of air velocity distribution in a multilayer conveyor dryer by computational fluid dynamics. Asia-Pacific Journal of Chemical Engineering, 2007, 2(2): 108-17. https://doi.org/10.1002/apj.48

[4] Jayaraman K S, Gupta D K D. Drying of fruits and vegetables. Handbook of industrial drying. CRC Press, 2020: 643-690. (In Chinese). https://doi.org/10.1201/9780429289774-21

[5] M.A. Hossain, B.K. Bala, M.A. Satter. Simulation of natural air drying of maize in cribs. Simulation Modelling Practice and Theory, 2003, 11(7): 571-583. https://doi.org/10.1016/j.simpat.2003.08.003

[6] Mikulec M, Piehl H. Verification and validation of CFD simulations with full-scale ship speed/power trial data. Brodogradnja, 2023, 74(1):41-62. https://doi.org/10.21278/brod74103

[7] Cupek J, Tkadlecková M, Merder T, Walek J, Saternus M, Pieprzyca J. Computational fluid dynamics (CFD) analysis of medium flow and removal of inclusions in a two-strand tundish. Metalurgija, 2023, 62(3-4):335-338.

[8] Jiang, Q., Zhang, Y., Yan, S., & Xu, L. (2021). Optimal design of an angular box for a mixed flow grain dryer. Applied Engineering in Agriculture, 37(4), 555-562. The USA. https://doi.org/10.13031/aea.14643

[9] Chaven A, Vitankar V, Shinde N, et al. CFD simulation of solar grain dryer. Drying Technology, 2021, 39(8): 1101-13. https://doi.org/10.1080/07373937.2020.1863422

[10] V.M. Romero. CerezoM.I. GarciaM.H. Sanchez. Simulation and validation of vanilla drying process in an indirect solar dryer prototype using CFD fluent program. Energy Procedia,2014,57 :1651-1658. https://doi.org/10.1016/j.egypro.2014.10.156

[11] Yue X, Zhao J, Shi E, et al. Analysis of air velocity distribution in a multilayer conveyor dryer by computational fluid dynamics. Asia-Pacific Journal of Chemical Engineering, 2007, 2(2): 108-17. https://doi.org/10.1002/apj.48

[12] Zhang P, Mu Y, Shi Z, et al. Computational fluid dynamic analysis of airflow in belt dryer: effects of conveyor position on airflow distribution. Energy Procedia, 2017, 142: 1367-74. https://doi.org/10.1016/j.egypro.2017.12.521

[13] Zhang P, Wu P, Zhang Q, et al. Optimization of feed thickness on the distribution of airflow velocity in belt dryer using computational fluid dynamics. Energy Procedia, 2017, 142: 1595-602. https://doi.org/10.1016/j.egypro.2017.12.536

[14] Zhang Q, Huang M, Wang J, et al. Investigation on airflow distribution under different feed thicknesses combined with CFD modeling and experimental verification. Drying Technology, 2020, 39(3): 306-23. https://doi.org/10.1080/07373937.2020.1777561

[15] Huang D, Men K, Tang X, et al. Microwave intermittent drying characteristics of camellia oleifera seeds. Journal of Food Process Engineering, 2021, 44(1): e13608. https://doi.org/10.1111/jfpe.13608

[16] Huang D, Tao Y, Li W, et al. Heat transfer characteristics and kinetics of Camellia oleifera seeds during hot-air drying. Journal of Thermal Science and Engineering Applications, 2020, 12(3): 031017. https://doi.org/10.1115/1.4045118

[17] Li J, Zhao P, Shi Y, et al. Analysis of transient inhomogeneous flow and thermal characteristics in a drying room via large eddy simulation. Chemical Engineering & Technology, 2020, 43(7): 1372-1382. https://doi.org/10.1002/ceat.201900661

[18] Zhang Y, Jiang Q, Liangyuan X U, et al. Mutil-objective optimization of hot blast stove heat exchanger. INMATEH-Agricultural Engineering, 2023, 69(1). https://doi.org/10.35633/inmateh-69-23

[19] Nanvakenari S, Movagharnejad K, Latifi A. Multi-objective optimization of hybrid microwave-fluidized bed drying conditions of rice using response surface methodology. Journal of Stored Products Research, 2022, 97: 101956. https://doi.org/10.1016/j.jspr.2022.101956

[20] Howard D A, Jørgensen B N, Ma Z. Multi-Method simulation and multi-objective optimization for energy-flexibility-potential assessment of food-production process cooling. Energies, 2023, 16(3): 1514. https://doi.org/10.3390/en16031514

[21] Kiranoudis C T, Maroulis Z B, Marinos-Kouris D. Product quality multi-objective dryer design. Drying technology, 1999, 17(10): 2251-2270. https://doi.org/10.1080/07373939908917682

[22] Iranmanesh M, Akhijahani H S, Jahromi M S B. CFD modeling and evaluation of the performance of a solar cabinet dryer equipped with evacuated tube solar collector and thermal storage system. Renewable Energy, 2020, 145: 1192-1213. https://doi.org/10.1016/j.renene.2019.06.038

[23] Singh S. Experimental and numerical investigations of a single and double pass porous serpentine wavy wire mesh packed bed solar air heater. Renewable Energy, 2020, 145: 1361-1387. https://doi.org/10.1016/j.renene.2019.06.137

[24] Amanlou Y, Zomorodian A. Applying CFD for designing a new fruit cabinet dryer. Journal of Food Engineering, 2010, 101(1): 8-15. https://doi.org/10.1016/j.jfoodeng.2010.06.001

[25] Zhao L, Li Y. Wind load of low-rise building based on fluent equilibrium atmospheric boundary layer. Tehnički vjesnik, 2023, 30(4): 1274-1282. https://doi.org/10.17559/TV-20230205000324

[26] Jiang Q, Zhang Y, Yan S, et al. Optimal Design of an Angular Box for a Mixed Flow Grain Dryer. Applied Engineering in Agriculture, 2021, 37(4) : 555-562. https://doi.org/10.13031/aea.14643

[27] Menter F R. Two-equation eddy-viscosity turbulence models for engineering applications. AIAA journal, 1994, 32(8): 1598-1605. https://doi.org/10.2514/3.12149

[28] Menter F R, Kuntz M, Langtry R. Ten years of industrial experience with the SST turbulence model. Turbulence, heat and mass transfer, 2003, 4(1): 625-632.

[29] Galamboš S, Poznanović N, Nikolić N, et al. Experimental and numerical studies on improvement of aerodynamic performance of a semi-trailer truck model using the cabin spoiler. Tehnički vjesnik, 2022, 29(6): 1991-2000. https://doi.org/10.17559/TV-20211025173605

[30] Zhu Y, Wang P, Sun D, et al. Multiphase porous media model with thermo-hydro and mechanical bidirectional coupling for food convective drying. International Journal of Heat and Mass Transfer, 2021, 175: 121356. https://doi.org/10.1016/j.ijheatmasstransfer.2021.121356

[31] Mackowiak J. Fluid dynamics of packed columns. Chemische Technik. Verfahrenstechnik. Springer-Verlag Berlin Heidelberg, 2010. https://doi.org/10.1007/b98397

[32] Das S, Deen N G, Kuipers J A M. Multiscale modeling of fixed-bed reactors with porous (open-cell foam) non-spherical particles: Hydrodynamics. Chemical Engineering Journal, 2018, 334: 741-759. https://doi.org/10.1016/j.cej.2017.10.047

[33] Zheng M, Wang Y, Teng H. Hybrid of" Intersection" algorithm for multi-objective optimization with response surface methodology and its application. Tehnički glasnik, 2022, 16(4): 454-457. https://doi.org/10.31803/tg-20210930051227

[34] Wu Min, Duan Hao, Wang Zhenwen et al. Design and test of infrared hot air combined dryer based on temperature and humidity control. Journal of Agricultural Machinery, 2020, 51(S1): 483-492. (In Chinese)

[35] Hou S, Zhang Z, Lian H, Xing X, Gong H, Xu X. Hull Shape Optimization of Small Underwater Vehicle Based on Kriging-Based Response Surface Method and Multi-Objective Optimization Algorithm. Brodogradnja, 2022, 73(3):111-134. https://doi.org/10.21278/brod73307

[36] Rafizadeh H, Azimifar F, Foode P, et al. Wrinkling prediction in deep drawing by using response surface methodology and artificial neural network. Transactions of FAMENA, 2017, 41(2): 17-28. https://doi.org/10.21278/TOF.41202

[37] Gong Zhongliang, Wang Pengkai, Li Dapeng et al. Heat flow field analysis and structure optimization of mesh belt dryer in multi-temperature zone. Transactions of the Chinese Society of Agricultural Engineering, 201,37(18):40-47. (In Chinese)

[38] Zheng M, Yu J. A Novel Method for Solving Multi-objective Shortest Path Problem in Respect of Probability Theory. Tehnički glasnik, 2023, 17(4):497-500. https://doi.org/10.31803/tg-20221026174845

Submitted: 27.8.2023

Accepted: 02.02.2024

Xiaobo Zhang
Huasheng Gan
Huazheng Xue
Qing Jiang*
College of Engineering, Anhui Agricultural University, Hefei, China
*Corresponding author:
jtao@ahau.edu.cn